2022-01-0556 Published 29 Mar 2022

Modeling of Regeneration Dynamics in Gasoline Particulate Filters and Sensitivity Analysis of Numerical Solutions

Kelsey Levine Cornell University

Gabriele Pozzato and Simona Onori Stanford University

Citation: Levine, K., Pozzato, G., and Onori, S., "Modeling of Regeneration Dynamics in Gasoline Particulate Filters and Sensitivity Analysis of Numerical Solutions," SAE Technical Paper 2022-01-0556, 2022, doi:10.4271/2022-01-0556.

Received: 18 Jan 2022 Revised: 18 Jan 2022 Accepted: 14 Jan 2022

Abstract

Gasoline direct-injection (GDI) engine technology improves vehicle fuel economy while decreasing CO_2 emissions. The main drawback of GDI technology is the increase in particulate emissions compared to the commonly used port fuel injection technologies. Today's adopted strategy to limit such emissions relies upon the use of aftertreatment gasoline particulate filters (GPFs). GPFs reduce particulates resulting from fuel combustion. Soot oxidation (also known as regeneration) is required at regular intervals to clean the filter, maintain a consistent soot trapping efficiency, and avoid the formation of soot plugs in the GPF channels. In this paper, starting from a multiphysics GPF model accounting for mass, momentum, and energy transport, a sensitivity analysis is carried out to choose the best mesh refinement, time step, and relative tolerance to ensure a stable numerical solution of the transport equations during regeneration while maintaining low computational time. Moreover, the numerical solutions are analyzed with respect to different smoothing of the model inputs, namely, experimental exhaust gas temperature, mass flow rate, and air-fuel ratio.

1. Introduction

The increasingly urgent threat of climate change necessitates rapid societal mobilization to reduce greenhouse gas emissions. The transportation industry is a significant contributor to greenhouse gas emissions, accounting for one-fifth of global emissions and nearly one-third of emissions in industrialized countries [1]. Researchers are actively investigating strategies for reducing vehicular greenhouse gas emissions. One such option is the adoption of gasoline direct injection (GDI) engines. GDI engines have a few key differences compared to conventional port-fuel injection (PFI) engine technology; in the former, fuel is injected directly into the engine cylinders, whereas in the latter, fuel is mixed with air before being injected into the cylinders. GDI engines reduce carbon dioxide emissions by up to 14% and improve fuel economy by up to 8% [2,3]. Because of these benefits, GDI-equipped engines are rapidly growing in popularity. Over the six-year period between 2009 and 2015, the percentage of GDI vehicles in the United States increased from less than 5% to 46%, and the EPA projects that GDI engines will power 93% of vehicles in the United States by 2025 [2,4].

Despite their rising popularity and significant fuel economy benefits, GDI engines have the significant drawback of producing more particulate pollution. Black carbon, which makes up a large portion of the particulate pollution from GDI vehicles, causes a warming effect by absorbing sunlight and reducing the albedo of the planet. Recent studies suggest that high emissions of these sunlight-absorbing particulates counteract the improvement in fuel economy so that implementation of GDI engines can result in a net warming effect [2,4]. Zimmerman et al. suggest that using GDI engine technology must result in an improvement in fuel economy by as much as 26% to negate the warming effects from increased black carbon emissions [2]. Saliba *et al.* tested a fleet of 82 light-duty gasoline vehicles spanning a range of model years, vehicle types, emissions certification standards, and manufacturers. They found that a 1.6% increase in fuel economy was sufficient to offset warming effects of increased black carbon pollution. However, they noted that increased black carbon pollution from GDI engines lowers their potential climate benefits by 10-20% [4].

Particulate emissions have negative impacts on local environmental and human health. They are linked to increased rates of cancer, respiratory disease, throat and eye irritation, cardiovascular effects such as arrhythmia and heart attacks, and premature death. They have also been shown to cause birth defects and growth retardation in newborn children [5]. Soot particle emissions are also detrimental to the environment; they contribute to acid rain, increase the acidity of water, change the nutrient balance in drainage basins and coastal waters, decrease nutrient content in soil, and damage forest ecosystems and agricultural fields [6].

In Europe, the problem of increased particulate emissions from GDI engines was addressed with the establishment of the EURO 6 standard in 2016. This regulation limited particulate mass (PM) emissions to the EURO 5 level and introduced particulate number (PN) emissions for GDI engines (both equivalent to the limits set for diesel vehicles) [7]. PM/PN regulations were introduced in China with the implementation of the CN6a standard in July 2020. This limits PM emissions to 0.0045 g/km and PN emissions to 6.0×10^{11} particles/km, which is comparable in stringency to EURO 6. In July 2023, the CN6b standard will impose even tighter limitations on particulate pollution, requiring PM emissions to be lowered to 0.003 g/km [8]. No PM/PN particulate regulation is actively in place in the United States at the time this paper was written.

GDI engines can be equipped with aftertreatment devices such as gasoline particulate filters (GPFs) to trap particulate matter. Regulations in Europe and China may necessitate the use of GPFs in GDI-equipped engines to meet emissions limits. Although comparable standards have not been established in the United States, we strongly believe that, in the pursuit of a more sustainable future, research on pollutant mitigation and effective aftertreatment devices is of paramount importance and should never stop. This is particularly true given the recent outlooks showing that conventional and hybrid vehicles are projected to lead the market until 2040 [9].

The geometric structure and design of GPFs are similar to that of diesel particulate filters (DPFs). However, while the mechanics and working principles of DPFs are well established in the literature [29], research on GPFs is comparatively lagging. There are some key differences between the operation of a GPF and a DPF; for example, gasoline engines typically emit smaller soot particles than diesel engines, and the exhaust has a lower oxygen content and higher temperature [10]. This means that findings from investigations on diesel filters are not necessarily applicable to GPFs, hence research specific to GPFs is necessary.

Recent studies have attempted to characterize effects of operational parameters on GPFs. Xie *et al.* investigated the effect of electric regeneration on combustion performance and soot oxidation of a coated GPF [11]. They created an improved GPF design where exhaust is heated directly in the gap area between the carrier and the filter. They varied the electric heating power and measured the corresponding soot oxidation rate, pressure drop, soot mass concentration, and NO_2 mass fraction. They found that their improved design resulted in a 4.1% increase in soot oxidation rate while the length and volume of the filter were reduced, and the pressure drop remained about the same. In a subsequent investigation, they found that using lower exhaust flow rates, higher exhaust temperatures, and higher exhaust oxygen and NO concentrations increased the soot oxidation rate and lowered the required heating power [12]. Lowering the flow rate and increasing the temperature was found to have significant effects on heating power than adjusting the concentration of oxygen or NO. Zuo et al. studied how regeneration temperature and pressure growth rate varied with different exhaust parameters (exhaust temperature, exhaust flow rate, oxygen concentration, and α, the ratio of NO_2 mass fraction to particulate mass fraction) [13]. They found that lower values of α, higher exhaust temperatures, lower regeneration temperatures, and lower oxygen concentrations increased the pressure growth rate. They also showed that increasing oxygen concentration reduced temperature and pressure drop in the regeneration equilibrium state. Zuo *et al.* measured the effect of four different parameters (exhaust temperature, exhaust flow rate, oxygen concentration, and NO_2/NO ratio) on catalytic efficiency in a coated GPF [14]. In the range 520 - 740 K, they found that a middle temperature of 600 K, lower flow rates, higher oxygen concentrations, and increased NO_2 concentrations maximized catalytic efficiency.

Rathod et al. [15] studied the effect of soot loading on pressure drop and trapping efficiency in GPFs. According to their work, the wall porosity decreases, and the trapping efficiency increases as soot loading increases. This occurs because the accumulated soot blocks additional particles as the exhaust flows through the filter. However, the reduction in porosity also slows the flow of the exhaust gas through the filter, which leads to an increase in backpressure and large pressure drops across the filter. This can lead to overheating, cracks, or even melting of the thermal substrate [16]. Therefore, regeneration to burn off the accumulated soot particles that would otherwise obstruct the flow of exhaust through the filter is key. The regeneration process is currently not well characterized in the literature, and it is critical to maintain high trapping efficiency while ensuring thermal stability of the filter [28].

In this work, starting from the 2-D model of an uncoated gasoline particulate filter developed by Pozzato *et al.* in COMSOL Multiphysics [17], we enhance the model to incorporate the regeneration dynamics and perform a model sensitivity analysis with respect to three solver settings: mesh size, relative tolerance, and time step. Moreover, we analyze the effect of smoothing the experimental input data on convergence. Ultimately, this work provides useful insights for an effective numerical solution of the energy, mass, and momentum transport equations of the GPF model. This is the enabling step for the use of the model for the characterization of temperature gradients across the filter during regeneration which is necessary to understand and avert the formation of fractures or device failures.

The remainder of the paper is organized as follows. In Section 2, the experimental setup is described. In Section 3, we show the underlying physics and formulate balance equations for the GPF COMSOL model. In Sections 4 and 5, the sensitivity and input smoothing analysis are described. Lastly, in Section 6 we justify our choices for the solver settings and smoothing frequency.

2. Experimental Setup

Experiments used for the development of the GPF model are performed on a 2.0 L, 4-cylinder, turbocharged, GDI engine. The vehicle is equipped with a GPF 300/8, provided by *Corning*, positioned downstream of the three-way catalytic converter (TWC). The GPF, composed of cordierite, is characterized by 2534 channels and a trapping efficiency of 0.725 L. The filter is equipped with 23 K-type thermocouples disposed in two planes (each plane has 13 thermocouples, with the centerline thermocouples shared between the two planes). Two exposed

junction J-type thermocouples are utilized to measure the inlet and outlet temperatures. Upstream of the GPF, a wide band λ sensor is used to analyze the exhaust gas composition. For additional details on the experimental setup, readers are referred to [15]. Geometrical and physical properties of the filter are summarized at the end of the paper, in the Definitions/Abbreviations section.

2.1. Regeneration Experiment

Starting with the vehicle and engine at room temperature, 20°C (293.15 K), the vehicle is first kept in idling conditions. Secondly, the vehicle is accelerated until the inlet temperature of the GPF reached 700°C (973.15 K). At that point, as the throttle tip-out occurred, the fuel is cut. As the engine and vehicle speeds started decreasing (coasting), oxygen is fed to the GPF from the engine. Regeneration is now taking place according to the following reaction paths:

$$C + O_2 \rightarrow CO_2$$

$$C + 0.5O_2 \rightarrow CO$$

An example of the tip-out procedure is shown in Figure 1. The inlet temperature (T_{inlet}), air-fuel ratio λ (used to compute the volume fractions X_i of N_2, H_2O, CO_2, and O_2 as in [17]), and inlet mass air flow ($\dot{m}_{inlet}$) are used as inputs for the model described in the next section.

FIGURE 1 GPF inlet temperature, mass air flow, and λ during a throttle tip-out regeneration test.

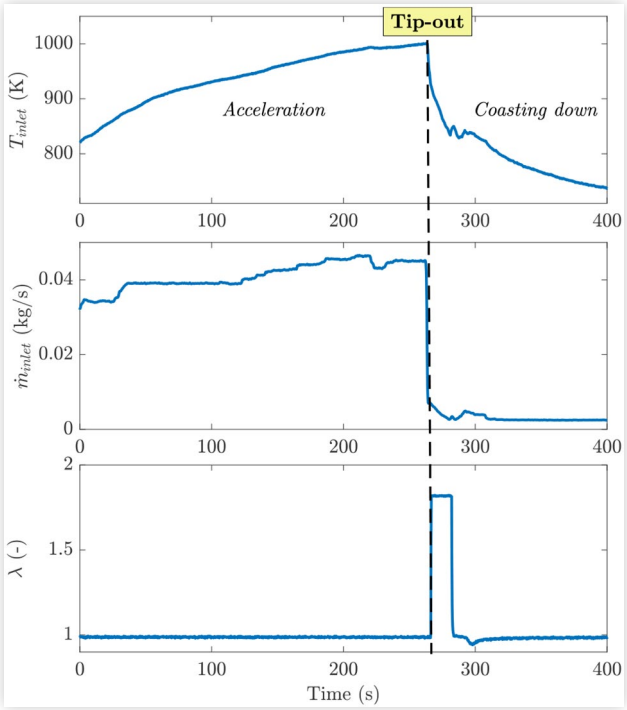

FIGURE 2 Geometry of the filter (top) with a slice composed of 47 channels (bottom) as in [17]. Red circles highlight locations along the centerline. D and L are the filter diameter and length, respectively.

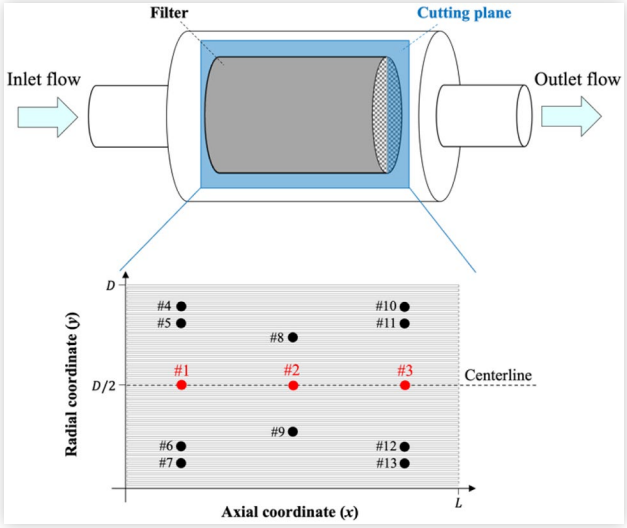

3. Modeling

The 2D physics-based GPF model used in this work, previously developed in [17], accounts for mass, energy, and momentum transport dynamics along both axial (x) and radial (y) coordinates. As shown in Figure 2, the model considers a slice of the filter, composed of 47 channels and corresponding to one of the two planes in which 13 K-type thermocouples are disposed. The geometry of a single channel is shown in Figure 3 with specific sections of the domain (inlet and outlet channels, wall, plug, and soot layer) labeled as 1, 2, 3, and 4, respectively. First, the exhaust gas enters the filter through the inlet channel. Secondly, the gas is forced to flow inside the wall, which stops the soot particulates from being released into the atmosphere. The accumulation of soot on top of the wall leads to the formation of a soot layer. Finally, the exhaust gas exits the filter through the outlet channel.

Exergy, mass, and momentum balance equations for inlet/outlet channels, walls, and plugs come from the clean filter studies in [17]. In this paper, the filter model is enhanced by modeling the regeneration dynamics in the soot layer. Energy, mass, and momentum balance in the soot layer are modeled according to Equations (6)-(15), (20)-(24), and (30)-(31), respectively.

3.1. Energy Balance

The energy balance is solved using the Heat Transfer in Fluids interface in COMSOL. The following heat balance equation is applied to the exhaust gas in the inlet and outlet channels (labeled as (1) in Figure 3):

$$\rho C_p \frac{\partial T}{\partial t} + \rho C_p (\boldsymbol{u} \cdot \nabla T = \nabla \cdot (k \nabla T) \quad (1)$$

where ρ is the exhaust gas density, C_p is the specific heat capacity, and k is the thermal conductivity of the exhaust gas

FIGURE 3 Section of one filter channel.

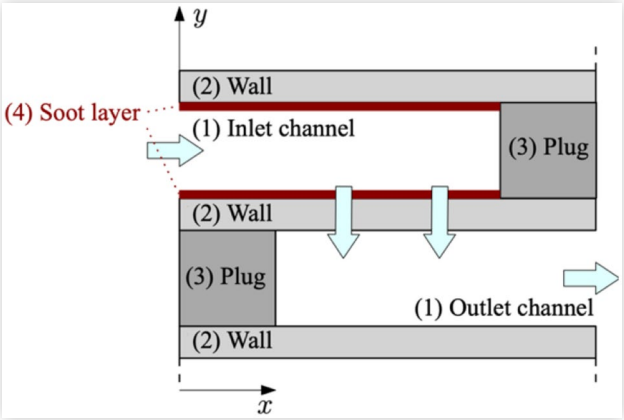

(determined by COMSOL). T is the exhaust gas temperature, and $\boldsymbol{u}$ is the exhaust gas speed.

The wall (labeled as (2) in Figure 3) is modeled as a porous medium in which solid (cordierite) and gaseous (exhaust gas) phases coexist:

$$\left(\rho C_p\right)_{eff}\frac{\partial T}{\partial t}+\rho C_p\left(\boldsymbol{v}\cdot\nabla T\right)=\nabla\cdot\left(k_{eff}\nabla T\right) \tag{2}$$

$$\left(\rho C_p\right)_{eff}=\left(1-\varepsilon_m\right)\rho_m C_m+\varepsilon_m\rho C_p \tag{3}$$

$$k_{eff}=\left(1-\varepsilon_m\right)k_m+\varepsilon_m k \tag{4}$$

In these equations, $\boldsymbol{v}$ is the Darcy average velocity, C_m is the specific heat capacity of the material (cordierite) determined by COMSOL, ε_m is the wall porosity, ρ_m is the cordierite density, and k_m is the cordierite thermal conductivity.

The following equation is applied to the channel plugs (labeled as (3) in Figure 3):

$$\rho_{plug}C_m\frac{\partial T}{\partial t}=\nabla\cdot\left(k_{plug}\nabla T\right) \tag{5}$$

where $\rho_{plug}=\rho_m\cdot(1-\varepsilon_p)$, $k_{plug}=(1-\varepsilon_p)\cdot k_m$, and ε_p is the plug porosity.

Similarly, the soot layer is modeled as a porous medium (labeled as (4) in Figure 3) in which solid (soot) and gaseous phases (exhaust gas) coexist:

$$\left(\rho C_p\right)_{eff}\frac{\partial T}{\partial t}+\rho C_p\left(\boldsymbol{v}\cdot\nabla T\right)=\nabla\cdot\left(k_{eff}\nabla T\right)+\dot{q} \tag{6}$$

$$\dot{q}=\sum_{j=1,2}r_j\Delta H_j \tag{7}$$

$$\left(\rho C_p\right)_{eff}=\rho_s C_s+\varepsilon_s\rho C_p, \tag{8}$$

$$k_{eff}=\left(1-\varepsilon_s\right)k_s+\varepsilon_s k \tag{9}$$

where ρ_s is the soot density, C_s is the soot specific heat capacity, ε_s is the soot porosity, and k_s is the soot thermal conductivity. ΔH_j is the enthalpy of reaction and r_j is the reaction rate for the following reaction paths:

$$1.C+O_2\rightarrow CO_2$$

$$r_1=\left(1-f_{CO}\right)\cdot A_1\cdot e^{-\frac{E_a}{R_{gas}\cdot T}}\cdot\left[O_2\right]\cdot\left[C\right]_s \tag{10}$$

$$2.C+0.5O_2\rightarrow CO$$

$$r_2=f_{CO}\cdot A_2\cdot e^{-\frac{E_a}{R_{gas}\cdot T}}\cdot\left[O_2\right]^{0.5}\cdot\left[C\right]_s \tag{11}$$

In the rate equations, $\left[C\right]_s=\frac{\rho_s}{M_c}$ is the concentration of carbon in the soot layer (M_c is the molecular weight of carbon) and $[O_2]$ is the concentration of the oxygen.

f_{CO} is the thermal selectivity [18, 19] defined as:

$$f_{CO}=\frac{1}{1+k_{ts}\cdot X_{O_2}^{q}\cdot e^{\frac{E_{ts}}{R_{gas}\cdot T}}} \tag{12}$$

where:

$$\frac{E_{ts}}{R}=3000\left[K\right] \tag{13}$$

$$q=0.21 \tag{14}$$

$$k_{ts}=0.02 \tag{15}$$

and X_{O2} is the volume fraction of oxygen in the exhaust gas.

The temperature boundary condition is set at the filter inlet, assuming a fully developed thermal flow:

$$T\left(y,t\right)\big|_{x=0}=bT_{inlet}\left(t\right)+\left(1-b\right)\cdot T_{inlet}\left(t\right)\cdot\left(1-\left(\frac{0.5D-y}{0.5D}\right)^2\right) \tag{16}$$

where b is the thermal distribution gain across the filter with a value of 0.9162, T_{inlet} is the inlet temperature (obtained experimentally), D is the filter diameter (116.52 mm), and y is the radial distance along the filter.

3.2. Mass Balance

The mass transport equations are solved with the Transport of Diluted Species interface in COMSOL, assuming N_2 and H_2O as inert species. The following mass balance equation is applied to the exhaust gas in the inlet and outlet channels:

$$\frac{\partial c_i}{\partial t}=-\boldsymbol{u}\cdot\nabla c_i+\nabla\cdot\left(D_i\nabla c_i\right)$$

$$i\in\left\{\mathrm{CO},\mathrm{CO_2},\mathrm{O_2}\right\} \tag{17}$$

where c_i and D_i are the concentration and diffusion coefficient of the i-th species, respectively.

The following mass balance equation is applied to the wall, where the exhaust gases are modeled in porous media:

$$\varepsilon_m\frac{\partial c_i}{\partial t}=-\boldsymbol{v}\cdot\nabla c_i+\nabla\cdot\left(D_{eff,i}\nabla c_i\right)$$

$$i\in\left\{\mathrm{CO_2},\mathrm{O_2},\mathrm{CO}\right\} \tag{18}$$

where $D_{eff,i}$ is the effective diffusion coefficient for species i in porous media, determined as follows:

$$D_{eff,i}=\frac{\varepsilon_m}{\tau_m}D_i \tag{19}$$

where τ_m is the wall tortuosity.

The plugs are considered a solid element, so there is no mass transport through them.

The following mass balance equation is applied to the soot layer:

$$\varepsilon_s \frac{\partial c_i}{\partial t} = -\boldsymbol{v}\cdot\nabla c_i + \nabla\cdot\left(D_{eff,i}\nabla c_i\right) + R_i$$

$$i \in \{CO_2, O_2, CO\} \tag{20}$$

The effective diffusion coefficient of species i in porous media is determined as follows:

$$D_{eff,i} = \frac{\varepsilon_s}{\tau_s} D_i \tag{21}$$

where τ_s is the soot layer tortuosity. The reaction rates for each species O_2, CO_2, and CO are given below:

$$R_{O_2} = -r_1 - 0.5 r_2, \tag{22}$$

$$R_{CO_2} = r_1, \tag{23}$$

$$R_{CO} = r_2. \tag{24}$$

r_1 and r_2 are the reaction rates defined in Equations (10) and (11).

The following equation is used to set boundary conditions and initial conditions for species concentrations:

$$c_i = \frac{X_i(t)\cdot\rho_{inlet}(t)}{M_{tot}(t)},\ i \in \{N_2, H_2O, CO_2, O_2\}$$

$$c_i = 0\ \text{mol/m}^3, \qquad i \in \{CO\} \tag{25}$$

In this equation, X_i is the volume fraction of species i, ρ_{inlet} is the exhaust gas density (Equation (34)), and $M_{tot}(t)$ is the exhaust gas molar mass (Equation (35)). The boundary conditions are applied to the open channels on the inlet side; the initial condition is set in the channels, walls, and soot layer by evaluating the above equation at the initial time.

3.3. Momentum Balance

The momentum transport equations are solved with the Free and Porous Media Flow interface in COMSOL. The following equation is applied to the exhaust gas in the inlet and outlet channels:

$$\rho\left(\frac{\partial \boldsymbol{u}}{\partial t} + \boldsymbol{u}\cdot\nabla\boldsymbol{u}\right) = -\nabla p + \mu\nabla^2\boldsymbol{u} \tag{26}$$

$$\nabla\cdot\boldsymbol{u} = 0 \tag{27}$$

where p is the exhaust gas pressure, and μ is the dynamic viscosity of the exhaust gas (determined by COMSOL).

The following mass balance equation is applied to the wall, where the exhaust gases are modeled in porous media:

$$\frac{\rho}{\varepsilon_m}\left(\frac{\partial \boldsymbol{v}}{\partial t} + \frac{\boldsymbol{v}}{\varepsilon_m}\cdot\nabla\boldsymbol{v}\right) = -\nabla p + \frac{\mu}{\varepsilon_m}\nabla^2\boldsymbol{v} - \frac{\mu}{\kappa_m}\boldsymbol{v} \tag{28}$$

$$\nabla\cdot\boldsymbol{v} = 0 \tag{29}$$

The plugs are considered a solid element, so there is no momentum transport through them.

The following equations are applied to the soot layer:

$$\frac{\rho}{\varepsilon_s}\left(\frac{\partial \boldsymbol{v}}{\partial t} + \frac{\boldsymbol{v}}{\varepsilon_s}\cdot\nabla\boldsymbol{v}\right) = -\nabla p + \frac{\mu}{\varepsilon_s}\nabla^2\boldsymbol{v} - \frac{\mu}{\kappa_s}\boldsymbol{v}, \tag{30}$$

$$\nabla\cdot\boldsymbol{v} = 0 \tag{31}$$

where κ_s is the soot permeability. The pressure is set to 1 atm across the filter (initial condition) and at the outlets of open channels (boundary condition).

The initial condition for the exhaust gas velocity across the filter is 0 m/s. The boundary condition for exhaust gas velocity is set at the inlets of open channels:

$$\boldsymbol{u}(y,t)\big|_{x=0} = u_x^{inlet}(y,t)\mathbf{i} + u_y^{inlet}\mathbf{j}$$

$$\begin{cases} u_x^{inlet}(y,t) = a\cdot v_{inlet}(t)\cdot\left(1 - \left(\dfrac{0.5D - y}{0.5D}\right)^2\right) \\ u_y^{inlet} = 0 \end{cases} \tag{32}$$

$$v_{inlet}(t) = \frac{\dot{m}_{inlet}(t)}{\rho_{inlet}(t)\cdot\pi\dfrac{(D/2)^2}{2}} \tag{33}$$

$$\rho_{inlet}(t) = \frac{P_{inlet} M_{tot}(t)}{R_{gas} T_{inlet}(t)} \tag{34}$$

$$M_{tot}(t) = \sum_i X_i(t)\cdot M_i,\ i \in \{N_2, H_2O, CO_2, O_2\} \tag{35}$$

where $\mathbf{i}$ and $\mathbf{j}$ are $\mathbb{R}^2$ unit vectors, a is the flow distribution gain with a value of 2, $\dot{m}_{inlet}$ is the mass air flow (experimentally determined), P_{inlet} is the inlet pressure (1 atm), and X_i and M_i are volume fraction and molar mass of each species.

4. Sensitivity Analysis

The choice of mesh size, relative tolerance, and time step can significantly affect the accuracy and speed of the COMSOL simulations.

In our analysis, we use a grid mesh to approximate the CAD geometry; an example with the coarsest mesh is shown in Figure 4. The mesh is necessary to discretize the geometry because the COMSOL solver is based on finite element methods. As the mesh size tends to zero, the result approaches the exact solution of the equations being solved [20]. However, a smaller mesh requires more time and computational resources to converge. Therefore, to ensure confidence in the model, it is necessary to test from progressively finer meshes and compare results [21].

The relative tolerance sets the threshold within which the relative error must fall for the COMSOL simulation to converge. The absolute tolerance is set by scaling the relative tolerance by a factor of 0.1. The initial value of the absolute tolerance is therefore one order of magnitude lower than the relative tolerance. The absolute tolerance is applied to scaled variables, which are scaled automatically by COMSOL to

FIGURE 4 Coarsest grid mesh (mesh ref. 0) with 4194 elements as part of the COMSOL filter geometry.

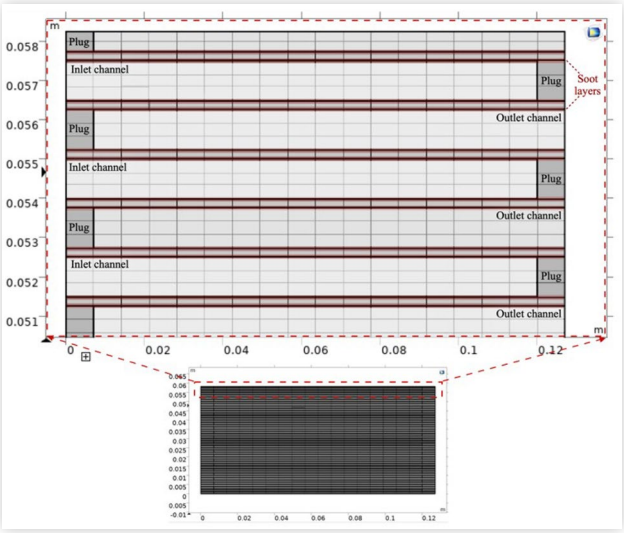

reconcile matrices for inputs of different magnitudes. As the simulation progresses, the absolute tolerance is set as the product of the relative tolerance and the change in a particular state [22]. Lowering the relative tolerance is likely to lead to a corresponding decrease in both absolute and relative error.

Lastly, the time step controls the intervals at which the steady-state solution of the Navier Stokes equation is estimated. From the model described in Section 2, the momentum transport equations (Navier Stokes and Hsu-Cheng) are decoupled from the energy and mass balance equations. This is reasonable because the thermal dynamics are significantly slower than fluid dynamics. The steady-state and transient equations are solved at each time step according to the flow chart in Figure 5. Starting from the initial condition IC at t = 0 s, the momentum balance equations are solved by the steady-state solver and the energy/mass balance equations are solved by the time dependent-solver. The time is increased by t_{step} and the final result of the current iteration becomes the new initial condition for the next iteration. Choosing a smaller time step generally increases the accuracy of the solution but requires higher computational effort.

Choosing a finer mesh with more elements and a lower relative tolerance will improve the accuracy of the simulation but will also require more time and memory to compute. Therefore, we performed a sensitivity analysis to validate the accuracy of the simulation while ensuring reasonable computational time. We tested mesh size, relative tolerance, and time step for all combinations of the settings shown in Table 1.

ref. = *'refinement'*

The sensitivity analysis is performed considering simulated temperatures at the 13 locations shown in Figure 2, which mirror the thermocouple locations in the physical experiments. We use the root-mean squared error (RMSE) to assess the performance of the model for different solver configurations. The RMSE was calculated as follows:

$$RMSE = \sum_{probe\in\{\#1,\#2,\#3\}} \sqrt{\frac{1}{N}\sum_{n=1}^{N}\left(T_{ref}^{sim}(n) - T^{sim}(n)\right)^2} \quad (36)$$

FIGURE 5 The flow chart indicates the role of the time step in controlling the intervals at which steady-state and time-dependent equations are solved. The end of the simulation is denoted by *tend*.

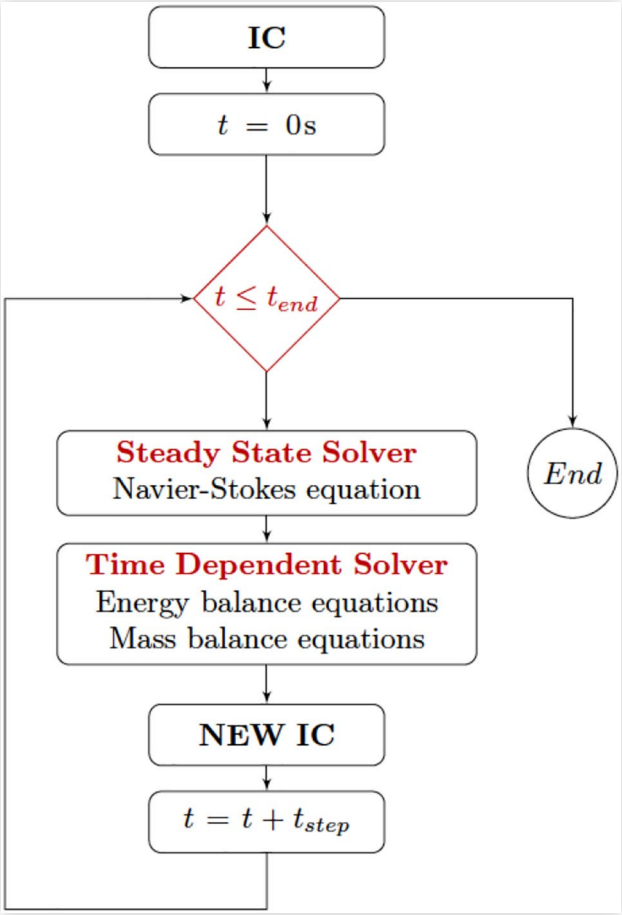

TABLE 1 Solver options for the sensitivity analysis.

Time step	Relative tolerance	Mesh size	Corresponding number of mesh elements
1.0 s	1e-2	ref. 0	4194
0.75 s	1e-3	ref. 1	16776
0.5 s	1e-4	ref. 2	67104
		ref. 3	268416

where N is the number of samples and T_{ref}^{sim} is the simulated temperature data from the most refined solution with the smallest relative tolerance (10^{-4}) and finest mesh (268416 elements). These settings for the relative error and mesh will lead to the most accurate solution. The RMSE is calculated with respect to the center probes (#1, #2, and #3), as they are characterized by higher temperature gradients and therefore are of increased interest.

5. Input Smoothing

Experimental data set composed of the exhaust mass air flow, inlet temperature, and volume fractions of N_2, H_2O, CO_2, and

O_2 (derived from λ according to [17]) is used as input to the model. COMSOL attempts to use Newton's method with this input data to solve a non-linear system of equations at every time step. However, this method can fail when there are strong nonlinearities or stiff behaviors in the input data [23]. Therefore, smoothing the input data can improve stability of the solver.

The following second order low-pass filter is used to smooth the experimental data:

$$LPF(s) = \frac{(2\pi f)^2}{s^2 + 2\xi\pi f\, s + (2\pi f)^2} \tag{37}$$

In this formulation, f is the cut-off frequency and ξ is the damping coefficient, chosen as 1 to avoid damping or amplification. It is critical to choose a low enough cut-off frequency to filter out nonlinearities, but not so low that information is removed from the experimental profile. The goal of the input smoothing is for the smoothed data to closely fit the experimental data and for the solver to reach convergence. A visual representation of the input smoothing for three different values of the cut-off frequency f (0.5, 1.0, and 1.5 Hz) is shown in Figure 6[1].

6. Results

6.1. Sensitivity Analysis

The main results of the sensitivity analysis are shown in Figure 7. Figure 7(a) (top) shows that increasing mesh refinement has the most significant effect on decreasing RMSE. Figure 7(b) (bottom) shows how the computational time increases for finer mesh size and lower relative tolerance. Interestingly, the computational time does not increase uniformly with increasing relative tolerance; there are significant spikes in computational time when the relative tolerance is increased to 10^{-4}. This result may be influenced by the geometry, physics, coupling method, nonlinearity of the problem, boundary conditions, initial conditions, and/or the solver configuration. There is not a single clear reason why increasing the relative tolerance to 10^{-4} results in such large increases in computational time. However, Figure 7(a) shows that increasing the relative tolerance from 10^{-2} to 10^{-4} for a given mesh refinement does not lead to a corresponding monotonic decrease in RMSE. We therefore set the relative tolerance above 10^{-4} to reduce simulation time without compromising the accuracy of the solution.

Figure 8 shows the comparison between T_{ref}^{sim} and T^{sim} for a time step of 0.75 seconds and relative tolerance of 10^{-3}. The reference simulated temperature T_{ref}^{sim} is obtained with the lowest relative tolerance 10^{-4} and mesh ref. 3. While increasing the mesh size, T^{sim} converges to T_{ref}^{sim}, leading to a decrease of the RMSE (computed as in Equation (36)).

The solver settings were chosen upon reviewing all solutions with computational times less than three hours. We chose three hours as the maximum simulation time because we plan to identify the unknown parameters of the model using Particle Swarm Optimization (PSO). The purpose of the identification is to determine the optimal soot loading profile and the pre-exponential Arrhenius factors for the soot oxidation reactions. While the PSO algorithm is an effective tool for analyzing parameter spaces in nonlinear models [24], it requires hundreds of simulations. Therefore, the simulation time is a concern and three hours is a good tradeoff for the problem at hand. Assuming 500 simulations, the identification routine would converge in, at most, two months[2]. Based on the results of the eighteen simulations that met this criterion, the following settings resulted in the lowest RMSE: 1.0 s time step, 10^{-3} relative tolerance, and mesh ref. 2. These settings were used for subsequent analyses.

FIGURE 6 Original unfiltered data (solid blue line) vs. filtered data (dashed lines) at 0.5, 1.0, and 1.5 Hz for the mass air flow.

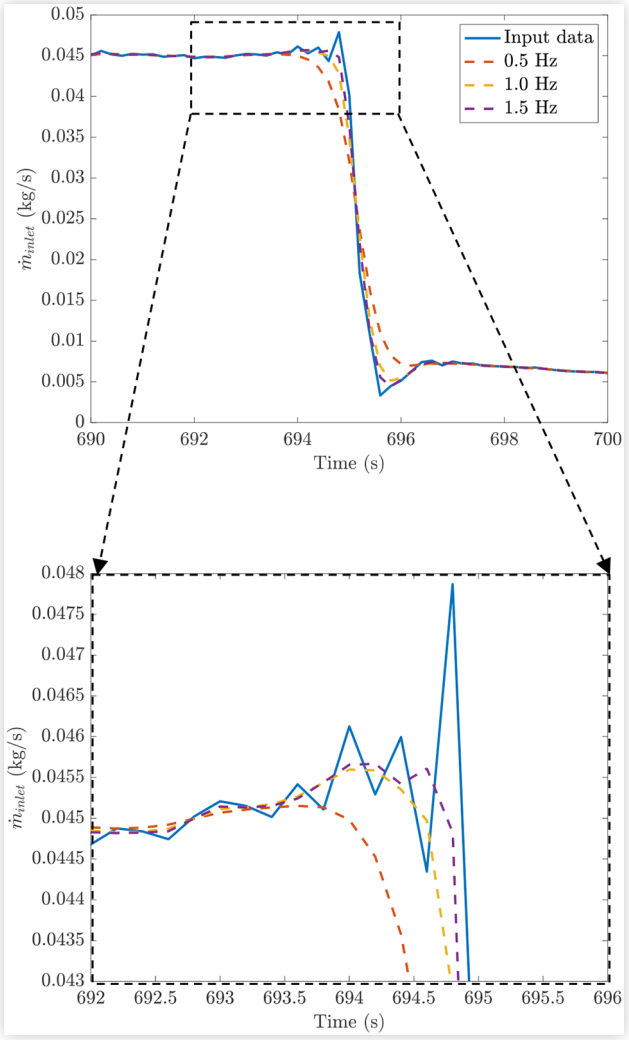

[1] The Matlab function *filtfilt* is used to filter the experimental data.

[2] The PSO convergence time is also a function of the initial guess and stopping criteria. On average, with a good initial guess and solver setting [10], convergence is expected within four weeks.

FIGURE 7 Comparison of (a) RMSE values, calculated with respect to the solution with the finest mesh and lowest relative tolerance, and (b) computational time for different solver settings. Missing data points indicate the COMSOL solver did not converge.

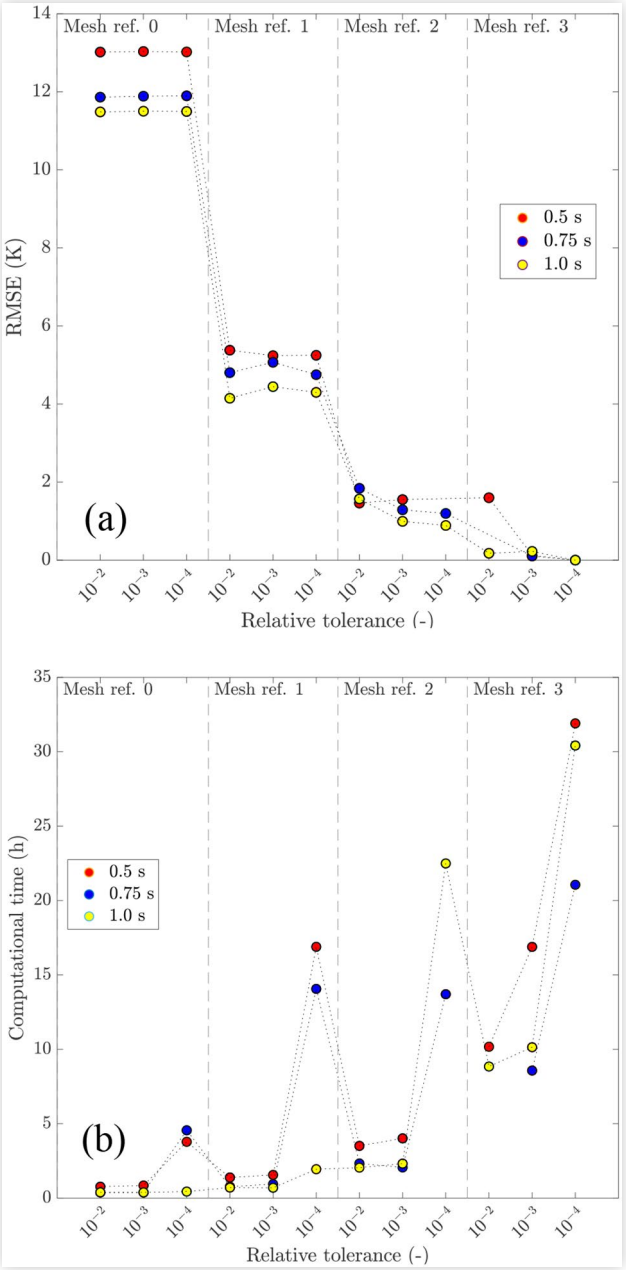

6.2. Input Smoothing

Figures 9-11 show the main results of the input smoothing at three different frequencies (0.5 Hz, 1.0 Hz, and 1.5 Hz). Figure 9 shows slight variations in temperature profile, but the trends are consistent for the three frequencies at the center of each plane.

Figure 10 shows that the maximum temperature at different locations in the filter does not vary significantly; additionally, Figure 11 shows minimal difference in computational time when the smoothing frequency is adjusted.

The 0.5 Hz frequency achieves the highest level of smoothing, which should help the solver converge to a more stable solution. Therefore, since no significant variation of the maximum temperature is shown in Figure 10, a conservative choice is made to smooth the input data with a cut-off frequency of 0.5 Hz.

FIGURE 8 Comparison between T_{ref}^{sim} and T_{sim} for a time step of 0.75 seconds and relative tolerance of 10^{-3}. The reference temperature T_{ref}^{sim} is computed with mesh ref. 3 and relative tolerance 10^{-4}. Only simulation results for probe #2 are shown.

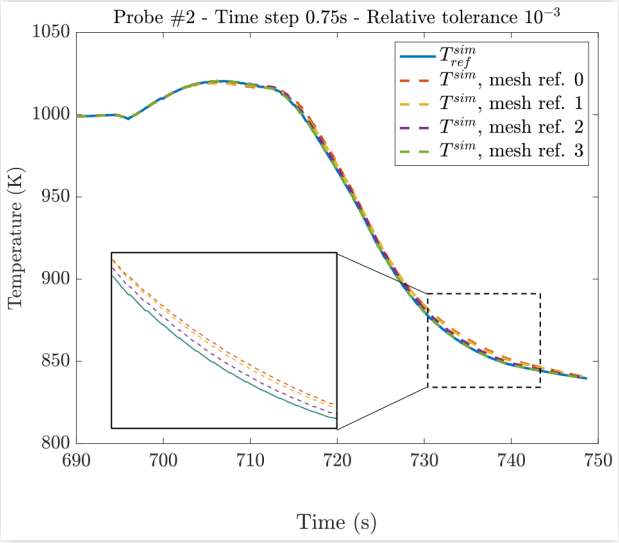

Summary/Conclusions

In this work, starting from a multi-physics model incorporating mass, energy, momentum, and soot burning dynamics, we performed a sensitivity analysis of the solver (with respect to mesh refinement, time step, and relative tolerance) and investigated the smoothing of the experimental data used as input to our model.

Sensitivity analysis - We tested four different mesh refinements, three different time steps, and three different values of the relative tolerance ranging from 10^{-2} to 10^{-4}. Our goal was to balance the requirement of low simulation time with minimal RMSE. We achieved 2.314-hour simulation time and 0.9933 RMSE with a mesh containing 67,104 elements, a time step of 1.0 seconds, and a relative tolerance of 10^{-3}. The sensitivity analysis gives us confidence in the accuracy of the model while keeping the simulation time within the specified timeframe. This is key to the identification we plan to complete, which requires a large number of simulations (on the order of 10^3).

FIGURE 9 Comparison of temperature results at the three chosen smoothing frequencies (0.5 Hz, 1.0 Hz, and 1.5 Hz).

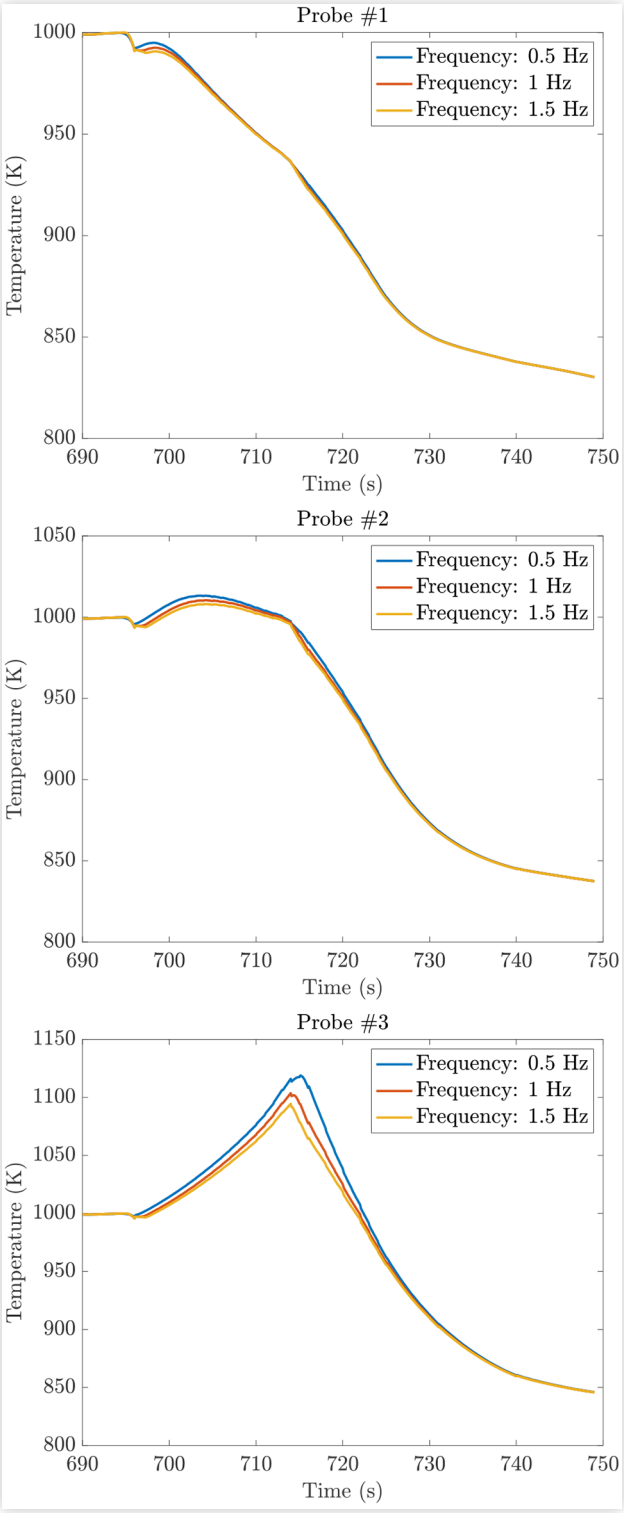

Input smoothing - We tested three different smoothing frequencies to filter nonlinearities from input data and improve solver convergence. We chose the lowest smoothing frequency (0.5 Hz) to increase the level of smoothing.

FIGURE 10 Comparison of simulated maximum temperatures over the time interval [690,749] s at all probe locations in Figure 2 and for each smoothing frequency.

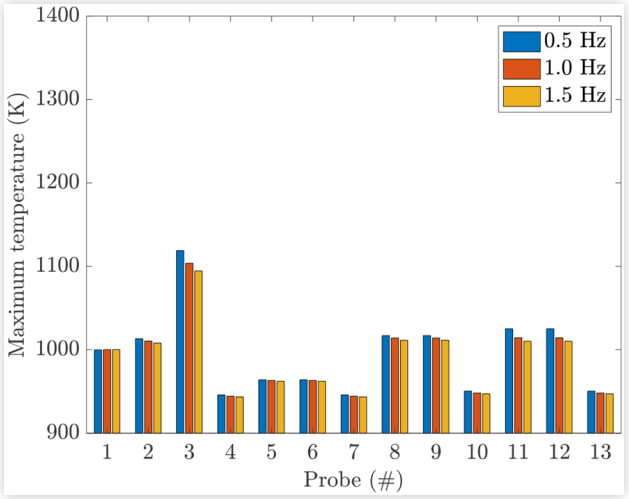

FIGURE 11 Comparison of computational time for the three smoothing frequencies 0.5, 1, and 1.5 Hz.

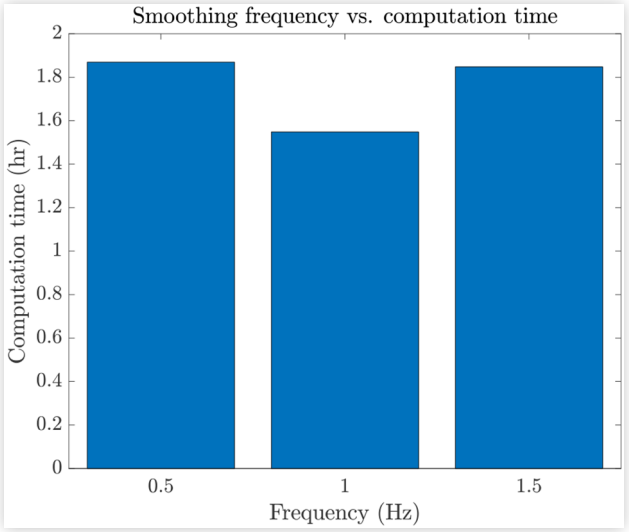

Future works will be devoted to the identification of the pre-exponential factors for the soot burning reactions.

References

1. Sperling, D., Cannon, J., and Lutsey, N., "Climate Change and Transportation," in *Reducing Climate Impacts in the Transportation Sector*, (Dordrecht: Springer, 2008), 1-14, doi:10.1007/978-1-4020-6979-6.
2. Zimmerman, N., Wang, J.M., Jeong, C., Wallace, J.S. et al., "Assessing the Climate Trade-Offs of Gasoline Direct Injection Engines," *Environ. Sci. Technol.* 50, no. 15 (2016): 8385-8392, doi:10.1021/acs.est.6b01800.

3. Neyestani, S.E., Walters, S., Pfister, G., Kooperman, G.J. et al., "Direct Radiative Effect and Public Health Implications of Aerosol Emissions Associated with Shifting to Gasoline Direct Injection Technologies in Light-Duty Vehicles in the United States," *Environ. Sci. Technol.* 54, no. 2 (2019): 687-696, doi:10.1021/acs.est.9b04115.
4. Saliba, G., Saleh, R., Zhao, Y., Presto, A.A., et al. "Comparison of Gasoline Direct-Injection (GDI) and Port Fuel Injection (PFI) Vehicle Emissions: Emission Certification Standards, Cold-Start, Secondary Organic Aerosol Formation Potential, and Potential Climate Impacts," *Environ. Sci. Technol.*, 51(11):6542-6552. doi:10.1021/acs.est.6b06509.
5. Prasad, R. and Bella, V.R., "A Review on Diesel Soot Emission, Its Effect and Control," *Bulletin of Chemical Reaction Engineering & Catalysis* 5, no. 2 (2010): 69-86, doi:10.9767/bcrec.5.2.794.69-86.
6. Environmental Protection Agency. n.d. "Health and Environmental Effects of Particulate Matter (PM)," https://www.epa.gov/pm-pollution/health-and-environmental-effects-particulate-matter-pm.
7. Williams, M., and Minjares, R. "A Technical Summary of Euro 6/IV Vehicle Emission Standards," International Council on Clean Transportation, June 2016. https://theicct.org/sites/default/files/publications/ICCT_Euro6-VI_briefing_jun2016.pdf.
8. International Council on Clean Transportation. "China's Stage 6 Emission Standard for New Light-Duty Vehicles (Final Rule)," March 2017. https://theicct.org/sites/default/files/publications/China-LDV-Stage-6_Policy-Update_ICCT_20032017_vF_corrected.pdf.
9. Bloomberg, N.E.F. "Electric Vehicle Outlook 2021," https://about.bnef.com/electric-vehicle-outlook/ (2021).
10. Arunachalam, H., Pozzato, G., Hoffman, M.A., and Onori, S., "Modeling the Thermal and Soot Oxidation Dynamics Inside a Ceria-Coated Gasoline Particulate Filter," *Control Engineering Practice* 94 (2020): 1-19, doi:10.1016/j.conengprac.2019.104199.
11. Xie, Y., Zuo, Q., Zhu, G., Guan, Q. et al., "Investigations on the Soot Combustion Performance Enhancement of an Improved Catalytic Gasoline Particulate Filter Regeneration System Under Different Electric Heating Powers," *Fuel* 283 (2020): 1-15, doi:10.1016/j/fuel.2020.119301.
12. Xie, Y., Zuo, Q., Wang, M., Wei, K. et al., "Effects Analysis on Soot Combustion Performance Enhancement of an Improved Catalytic Gasoline Particulate Filter Regeneration System with Electric Heating," *Fuel* 290 (2020): 1-16, doi:10.1016/j.fuel.2020.119975.
13. Zuo, Q., Zhu, X., Zhang, J., Zhang, B. et al., "Effects of Exhaust Parameters on Temperature and Pressure Drop of the Gasoline Particulate Filter in the Regeneration Equilibrium State," *Fuel* 257 (2019): 1-10, doi:10.1016/j.fuel.2019.116019.
14. Zuo, Q., Tang, Y., Chen, W., Zhang, J. et al., "Effects of Exhaust Parameters on Gasoline Soot Regeneration Performance of a Catalytic Gasoline Particulate Filter in Equilibrium State," *Fuel* 265 (2020): 1-13, doi:10.1016/j.fuel.2019.117001.
15. Rathod, D., Onori, S., Filipi, Z.., and Hoffman, M.. "Experimental Investigation of Soot Accumulation and Regeneration in a Catalyzed Gasoline Particulate Filter Utilizing Particulate Quantification and Gas Speciation Measurements," in *2018 ASME Internal Combustion Fall Technical Conference*, CA, Nov. 4-7, 2018.
16. Chan, T.W., Saffaripour, M., Liu, F., Hendren, J. et al., "Characterization of Real-Time Particle Emissions from a Gasoline Direct Injection Vehicle Equipped with a Catalyzed Gasoline Particulate Filter during Filter Regeneration," *Emiss. Control Sci. Technol.* 2 (2016): 75-88, doi:10.1007/s40825-016-0033-3.
17. Pozzato, G., Hoffman, M.A., and Onori, S. "*Multi-Channel Physics-Based Modeling and Experimental Validation of an Uncoated Gasoline Particulate Filter in Clean Operating Conditions*," in *2017 American Control Conference*, (ACC), IEEE, 2017.
18. Konstandopoulos, A.G. and Kostoglou, M., "Reciprocating Flow Regeneration of Soot Filters," *Combustion and Flame* 121, no. 3 (2000): 448-500, doi:10.1016/S0010-2180(99)00156-X.
19. Lee, S., Jeong, S., and Kim, W., "Numerical Design of the Diesel Particulate Filter for Optimum Thermal Performances During Regeneration," *Applied Energy* 86, no. 7 (2009): 1124-1135, doi:10.1016/k/apenergy.2008.07.002.
20. Nine, Bethany. "How to Implement a Mesh Refinement Study," COMSOL Blog (blog). August 6, 2013, https://www.comsol.com/blogs/how-to-implement-mesh-refinement-study/.
21. "Performing a Mesh Refinement Study," COMSOL, https://www.comsol.com/support/knowledgebase/1261, accessed September 19, 2021.
22. "Variable Step Solvers in Simulink," MathWorks, https://www.mathworks.com/help/simulink/ug/variable-step-solvers-in-simulink-1.html#f11-44943, accessed August 23, 2021.
23. "Improving Convergence in Nonlinear Time Dependent Models," COMSOL, https://www.comsol.com/support/knowledgebase/1127, accessed September 19, 2021.
24. Ebbesen, S., Kiwitz, P., and Guzzella, L.. "A Generic Particle Swarm Optimization Matlab Function," in *2012 American Control Conference (AAC)*, 1519-1524, 2012, doi:10.1109/ACC.2012.6314697.
25. Kröcher, O., Elsener, M., and Votsmeier, M., "Determination of Effective Diffusion Coefficients Through the Walls of Coated Diesel Particulate Filters," *Industrial & Engineering Chemistry Research* 48, no. 23 (2009): 10746-10750, doi:10.1021/ie901269v.
26. Koltsakis, G.C. and Stamatelos, A.M., "Modes of Catalytic Regeneration in Diesel Particulate Filters," *Industrial & Engineering Chemistry Research* 36, no. 10 (1997): 4155-4165, doi:10.1021/ie970095m.
27. Nicolin, P., Rose, D., Kunath, F., and Boger, T., "Modeling of the Soot Oxidation in Gasoline Particulate Filters," *SAE International Journal of Engines2015-01-1048* 8, no. 3 (2015): 1253-1260. https://doi.org/10.4271/2015-01-1048.
28. Korneev, S. and Onori, S., "Modeling the Flow and Transport Dynamics in Gasoline Particulate Filters to Improve Filtration Efficiency," *J. Dyn. Sys., Meas., Control* 142, no. 6 (2020): 061006.
29. Konstandopoulos, A.G. et al., "Fundamental Studies of Diesel Particulate Filters: Transient Loading, Regeneration and Aging," *SAE Transactions 2000-01-1016* (2000): 683-705. https://doi.org/10.4271/2000-01-1016.

Contact Information

Simona Onori
Energy Resources Engineering, Stanford University, Stanford, CA 94305
sonori@stanford.edu

Gabriele Pozzato
Energy Resources Engineering, Stanford University, Stanford, CA 94305
gpozzato@stanford.edu

Acknowledgments

The authors gratefully acknowledge the support of Fiat Chrysler Automobiles (FCA) US LLC for granting permission to utilize experimental data from previous research collaboration.

Gabriele Pozzato and Simona Onori acknowledge the financial support of National Science Foundation (NSF), United States through the CAREER Award number CMMI-1839050.

Kelsey Levine acknowledges the financial support of the Stanford University Summer Undergraduate Research in Geoscience and Engineering (SURGE) Program 2021.

Definitions/Abbreviations

$\Delta H_j = \Delta H_j(x,y,t)$ - Enthalpy of reaction j [J/mol]
ε_m - Wall porosity, 0.65 [-]
ε_p - Plug porosity, 0.5 [-]
ε_s - Soot porosity, 0.937 [-]
κ_m - Cordierite permeability, 2.82×10^{-12} [m^2]
κ_s - Soot permeability, 2.273×10^{-14} [m^2]
λ - Air-fuel ratio, [-]
$\mu = \mu(x,y,t)$ - Dynamic viscosity of exhaust gas [Pa s]
$\rho = \rho(x,y,t)$ - Exhaust gas density [kg/m^3]
ρ_m - Cordierite density, 2500 [kg/m^3]
ρ_s - Soot packing density, 123.473 [kg/m^3]
τ_m - Cordierite tortuosity, 3.5 [-] [25]
τ_s - Soot tortuosity, 1 [-]
A_1 - Pre-exponential Arrhenius factor, 10^7 [m^3/(mol s)]
A_2 - Pre-exponential Arrhenius factor, 10^7 [$m^{1.5}$/($mol^{0.5}$ s)]
a - Flow distribution gain, 2 [-]
b - Thermal distribution gain, 0.9162 [-]
$c_i = c_i(x,y,t)$ - Concentration of species i [mol/m^3]
C_m - Cordierite specific heat capacity [J/(kg K)]
$C_p = C_p(x,y,t)$ - Exhaust gas specific heat capacity [J/(kg K)]
C_s - Soot specific heat capacity, 1510 [J/(kg K)] [26]
$[C]_s$ - Concentration of carbon in the soot layer [mol/m^3]
D - Filter diameter, 116.52 [mm]
$D_i = D_i(x,y,t)$ - Diffusion coefficient of species i [m^2/s]
d_{por} - Average pore size, 1.7×10^{-5} [m]
E_a - Activation energy, 150×10^3 [J/mol] [27]
h_c - Channel height, 1.03 [mm]
h_w - Wall thickness, 0.22 [mm]
h_s - Soot layer thickness, 8.97 [μm]
$k = k(x,y,t)$ - Exhaust gas thermal conductivity [W/(m K)]
k_m - Cordierite thermal conductivity, 1 [W/(m K)]
k_s - Soot thermal conductivity, 2.1 [W/(m K)] [26]
$\dot{m}_{inlet}$ - Mass air flow (experimentally determined) [kg/s]
L - Filter length, 127 [mm]
M_c - Molecular weight of carbon, 0.012 [kg/mol]
M_i - Molar mass of species i (experimentally determined) [kg/mol]
$p = p(x,y,t)$ - Exhaust gas pressure [atm]
P_{inlet} - Inlet pressure, 1 [atm]
$\dot{q} = \dot{q}(x,y,t)$ - Heat source from reactions [W/m^3]
$r_j = r_j(x,y,t)$ - Reaction rate j [mol/(m^3s)]
R_{gas} - Gas constant, 8.314 [J/(mol K)]
$T = T(x,y,t)$ - Exhaust gas temperature [K]
T_{inlet} - Inlet temperature (experimentally obtained) [K]
$u = u(x,y,t)$ - Exhaust gas velocity field [m/s]
$v = v(x,y,t)$ - Exhaust gas Darcy velocity field [m/s]
v_{inlet} - Exhaust gas velocity [m/s]
x - Axial coordinate [m]
X_i - Volume fraction of species i [-]
y - Radial coordinate [m]

ISSN 0148-7191